Journal of Pharmaceutical Analysis 14 (2024) 100932

Contents lists available at ScienceDirect

Journal of Pharmaceutical Analysis

journal homepage: www.elsevier.com/locate/jpa

Original article

In situ visualization of the cellular uptake and sub-cellular distribution of mussel oligosaccharides

Zhenjie Yu [a, 1], Huarong Shao [b, c, 1], Xintian Shao [d], Linyan Yu [a], Yanan Gao [a], Youxiao Ren [a], Fei Liu [b, f], Caicai Meng [d, *], Peixue Ling [b], Qixin Chen [a, e, **]

[a] *Key Laboratory for Biotechnology Drugs of National Health Commission, School of Pharmaceutical Sciences & Institute of Materia Medica, Medical Science and Technology Innovation Center, Shandong First Medical University & Shandong Academy of Medical Sciences, Jinan, 250117, China*
[b] *Key Laboratory of Biopharmaceuticals, Engineering Laboratory of Polysaccharide Drugs, National-Local Joint Engineering Laboratory of Polysaccharide Drugs, Shandong Academy of Pharmaceutical Science, Jinan, 250101, China*
[c] *Shenzhen Research Institute of Xiamen University, Shenzhen, Guangdong, 518057, China*
[d] *School of Life Sciences, Medical Science and Technology Innovation Center, Shandong First Medical University & Shandong Academy of Medical Sciences, Jinan, 250117, China*
[e] *Departments of Diagnostic Radiology, Surgery, Chemical and Biomolecular Engineering, and Biomedical Engineering, Yong Loo Lin School of Medicine and Faculty of Engineering, National University of Singapore, Singapore, 119074, Singapore*
[f] *School of Pharmaceutical Sciences, Shandong University, Jinan, 250101, China*

A R T I C L E I N F O

Article history:
Received 22 August 2023
Received in revised form
25 December 2023
Accepted 29 December 2023
Available online 4 January 2024

Keywords:
Cellular imaging
Fluorescence labeling
Mussel oligosaccharide
Lipid metabolism

A B S T R A C T

Unlike chemosynthetic drugs designed for specific molecular and disease targets, active small-molecule natural products typically have a wide range of bioactivities and multiple targets, necessitating extensive screening and development. To address this issue, we propose a strategy for the direct *in situ* micro-dynamic examination of potential drug candidates to rapidly identify their effects and mechanisms of action. As a proof-of-concept, we investigated the behavior of mussel oligosaccharide (MOS-1) by tracking the subcellular dynamics of fluorescently labeled MOS-1 in cultured cells. We recorded the entire dynamic process of the localization of fluorescein isothiocyanate (FITC)-MOS-1 to the lysosomes and visualized the distribution of the drug within the cell. Remarkably, lysosomes containing FITC-MOS-1 actively recruited lipid droplets, leading to fusion events and increased cellular lipid consumption. These drug behaviors confirmed MOS-1 is a candidate for the treatment of lipid-related diseases. Furthermore, in a high-fat HepG2 cell model and in high-fat diet-fed apolipoprotein E (*ApoE*)$^{-/-}$ mice, MOS-1 significantly promoted triglyceride degradation, reduced lipid droplet accumulation, lowered serum triglyceride levels, and mitigated liver damage and steatosis. Overall, our work supports the prioritization of *in situ* visual monitoring of drug location and distribution in subcellular compartments during the drug development phase, as this methodology contributes to the rapid identification of drug indications. Collectively, this methodology is significant for the screening and development of selective small-molecule drugs, and is expected to expedite the identification of candidate molecules with medicinal effects.

© 2024 The Authors. Published by Elsevier B.V. on behalf of Xi'an Jiaotong University. This is an open access article under the CC BY-NC-ND license (http://creativecommons.org/licenses/by-nc-nd/4.0/).

* Corresponding author.
** Corresponding author. Key Laboratory for Biotechnology Drugs of National Health Commission, School of Pharmaceutical Sciences & Institute of Materia Medica, Medical Science and Technology Innovation Center, Shandong First Medical University & Shandong Academy of Medical Sciences, Jinan, 250117, China.
E-mail addresses: mengcaicai@sdfmu.edu.cn (C. Meng), chenqixin@sdfmu.edu.cn (Q. Chen).
[1] Both authors contributed equally to this work.

https://doi.org/10.1016/j.jpha.2023.12.022
2095-1779/© 2024 The Authors. Published by Elsevier B.V. on behalf of Xi'an Jiaotong University. This is an open access article under the CC BY-NC-ND license (http://creativecommons.org/licenses/by-nc-nd/4.0/).

1. Introduction

Natural products (NPs) and their derivatives have long served as exceptional sources of candidate drugs, offering unprecedented opportunities for disease treatment [1–3]. These compounds are particularly important for the treatment of cancer (e.g., vincristine) [4] and certain cardiovascular diseases (e.g., statins) [5]. Unlike chemically synthesized drugs designed for specific targets [6], NPs often exhibit broad biological activities and interact with multiple targets, resulting in complex and diverse mechanisms of action [7,8]. These factors mean that treatment indications and appropriate research models are often poorly defined, leading to the need for extensive screening and the application of assays across multiple research domains.

Because of the potential complexity of the interactions between NPs and biological pathways, relevant experimental protocols require significant effort and are often associated with an increased risk of failure. Several modern research strategies, including high-throughput screening techniques [9], seek to identify diseases and indications for bioactive components of NPs. Technologies that combine fluorescent labeling with live-cell imaging [10–12] represent attractive cell-based strategies for use in NP-related research. Such studies involve real-time tracking of drug distribution within cells and subcellular compartments. This approach utilizes fluorescent dyes or proteins to label compounds [13], allowing non-invasive, real-time observation, and permitting detailed studies of the behavior of drugs in living systems. For example, in recent studies, such drug tracking techniques have revealed the pathways by which platinum moves among lysosomes, autolysosomes, and nuclei [14], identified the patterns of localization of dextran within mitochondria [15], and elucidated the mitochondrial-binding targets of magnoflorine [16]. Although these studies have elucidated the distribution and metabolism of compounds within subcellular compartments, they have primarily focused on validated indications. However, they also suggested that studies probing subcellular behavior would be useful for exploring the characteristics of less-studied NP compounds.

Polysaccharides are natural biopolymers that are widely used in various fields, especially biomedical applications, owing to their fascinating properties such as renewability, biodegradability, and biocompatibility [17–20]. Mussel polysaccharide α-D-glucan (MP-A) [21] is an NP isolated from *Mytilus coruscus*, which is distributed along the coastlines of the Yellow Sea in China, the Korean Peninsula, and Hokkaido, Japan. The unique sugar chain structure and branching patterns of MP-A strongly influence the biological activities of this polysaccharide, including antioxidant, anti-inflammatory, anticancer, and immunoregulatory effects. While substantial work [22–26] has elucidated the efficacy of MP-A, less attention has been paid to a related compound, mussel oligosaccharide (MOS-1). MOS-1 is a low-molecular-weight homo-oligosaccharide composed of glucose with various properties governed by its specific glycosidic bond connections and sugar chain lengths. Unfortunately, the current technologies are not suitable for directly determining the physiological effects of MOS-1. Therefore, a strategy for the rapid identification of appropriate research models and therapeutic targets is necessary to facilitate drug development.

To overcome this bottleneck in exploring the potential biological applications of NPs, we proposed a strategy for the direct *in situ* dynamic examination of promising drug candidates, enabling us to closely reveal their functions and mechanisms of action. Specifically, we suggest the use of fluorescent probes in combination with NPs to allow the real-time tracking of drug distribution within cells and subcellular compartments. Using this approach, we can accurately monitor drug distribution and study its effect impact on various target organelles, providing direct evidence that can be used to decipher potential mechanisms and explore the functional applications of NPs. Employing this strategy, we observed that MOS-1 modulates lipid droplets and affects lipid metabolism, thus offering promising prospects as a candidate therapeutic agent for the treatment of non-alcoholic fatty liver disease (NAFLD).

2. Materials and methods

2.1. General materials

Reagents and consumables, such as hexamethylene diamine, sodium cyanoborohydride, FITC, and the polyacrylamide coagulation column for synthesis, were purchased from Shanghai Macklin Biochemical Technology Co., Ltd. (Shanghai, China) and Shanghai Aladdin Biochemical Technology Co., Ltd. (Shanghai, China). MOS-1 was provided by Shandong Academy of Pharmaceutical Sciences (Jinan, China). Fetal bovine serum (FBS) was obtained from Shanghai VivaCell Biosciences Ltd. (Shanghai, China). Dulbecco's modified Eagle's medium (DMEM), penicillin-streptomycin (10,000 units/mL), trypsin-ethylenediamine tetraacetic acid (EDTA) phenol-free medium, and other reagents for cell culture were obtained from Gibco BRL Life Technologies Inc. (Grand Island, NY, USA). Lyso-Tracker Red (LTR), 4′,6-diamino-2-phenyl indole (DAPI), Hoechst (nuclei dye), Mito-Tracker Red (MTR), and Lyso-Tracker Deep Red (LTDR) were purchased from Invitrogen (Eugene, OR, USA). Lipid droplets dye (Lipi-Blue) was purchased from Dojindo Laboratories (Kumamoto, Japan). Lipid droplet plasmids labeled with red fluorescent protein (Plin2-mCherry) was obtained from Hanbio Biotechnology Co., Ltd. (Shanghai, China). The triglyceride (TG) content measurement kit was purchased from Biotopped Life Sciences (Beijing, China). Antibodies against LC3B and p62 were purchased from ABclonal Technology Co., Ltd. (Wuhan, China). The HepG2 cells were obtained from Fengshan Wang's laboratory of Shandong University (Jinan, China). HeLa cells were obtained from Xiaodong Mu's laboratory of Shandong First Medical University (Jinan, China). The U251 and MDA-MB-231 cells were obtained from Procell Life Science&Technology Co., Ltd. (Wuhan, China).

2.2. Synthesis and characterization of FITC-MOS-1

A mixture of mussel oligosaccharides (0.1 g, 0.15 mmol) and hexamethylene diamine (0.87 g, 7.48 mmol) were dissolved in 10 mL of glacial acetic acid, and the reducing agent sodium cyanide borohydride was added in the mixture, then heated to 45 °C for 10 h. After cooling to 25 °C, the solvent was removed by evaporation under reduced pressure, and the residue was filtered through a polyacrylamide gel column (Bio-Gel P-2) to remove the unreacted hexamethylene diamine and sodium cyanoborohydride. The product was characterized by high-resolution mass spectrometry (HRMS). The oligosaccharide hexamethylene diamine was dissolved in carbonate buffer (pH 9.0), then FITC dissolved in methanol was added, the mixture was heated to 45 °C for 14 h. The final product was separated and purified on a Bio-Gel P-2 column to obtain a brown solid. The final product was characterized by HRMS, proton magnetic resonance (^{1}H NMR), and carbon-13 nuclear magnetic resonance (^{13}C NMR).

2.3. Cell culture

HepG2, HeLa, U251, and MDA-MB-231 cells were all cultured in complete DMEM supplemented with 10% (*V*/*V*) FBS and penicillin-streptomycin (100 units/mL) in a 5% CO_2 humidified incubator at 37 °C.

2.4. Cytotoxicity assay

Cytotoxicity assays were performed using a Cell Counting Kit-8 (CCK-8) assay. HepG2 cells were seeded in 96-well plates at a density of 7×10^3 cells/well in DMEM with 10% (*V*/*V*) FBS and placed in an incubator (5% CO_2, 37 °C) for 24 h. The medium was replaced with 100 μL of fresh medium containing different concentrations (0.5, 1, 2.5, 5, 10, 20, and 30 μM) of FITC-MOS-1. After 24 h of incubation, 10 μL of CCK-8 solution was added to each well, followed by incubation for 2 h under the same conditions. After shaking for 2 h, the absorption wavelength of each well was measured at 450 nm by an enzyme labeling apparatus (BioTek Synergy HTX; Agilent Technologies, Inc., Beijing, China). Cell viability (%) was calculated by the mean absorbance value of the treatment group divided by the mean absorbance value of the control group [27,28].

2.5. Cell culture and imaging under confocal laser scanning microscopy or three-dimensional structured illumination microscopy (3D-SIM)

HepG2 cells were seeded at a density of 1×10^5 on 35 mm glass-bottom culture dishes and incubated with 2 mL of DMEM with 10% (*V*/*V*) FBS for 24 h incubation (5% CO_2, 37 °C). HepG2 cells were incubated with 10 μM FITC-MOS-1 for 30 min and washed with fresh DMEM for five times. Finally, the HepG2 cells were cultured in 1 mL of phenol-free medium and imaged using confocal laser scanning microscopy or 3D-SIM (Delta Vision, Inc., Issaquah, WA, USA). FITC-MOS-1 was excited at 488 nm and emitted at 490–550 nm.

2.6. Flow cytometry analysis

HepG2 cells were seeded in 6-well plates at a density of 1×10^5 cells/well in DMEM with 10% (*V*/*V*) FBS and placed in an incubator (5% CO_2, 37 °C) for 24 h. Then the culture medium was replaced with 1000 μL of fresh medium containing different concentrations (0, 5, 10, 20, and 30 μM) of FITC-MOS-1. Three secondary wells were created in each group. After staining with FITC-MOS-1 for 30 min, the cells were digested with trypsin and washed twice with precooled phosphate-buffered saline (PBS). The cells were resuspended with 500 μL of buffer and then detected by flow cytometry, and the medium culture was replaced with 10 μM FITC-MOS-1 for 0, 0.5, 1, 6, and 12 h, respectively. The cells were digested with trypsin and washed twice with precooled PBS. The cells were resuspended with 500 μL of buffer and then detected by flow cytometry.

2.7. Co-localization experiments

HepG2 cells were seeded at a density of 1×10^5 on 35 mm glass-bottom culture dishes and incubated with 2 mL of DMEM with 10% (*V*/*V*) FBS for 24 h incubation (5% CO_2, 37 °C). HepG2 cells were incubated with 10 μM FITC-MOS-1 for 30 min, 5 μM DAPI, 10 μM Hoechst, 100 nM LTR, 100 nM LTDR, and 100 nM Lipi-Blue for 30 min, respectively. The HepG2 cells were then washed five times with fresh DMEM. Finally, the HepG2 cells were cultured in 1 mL of phenol-free medium and imaged using confocal laser scanning microscopy or 3D-SIM (Delta Vision, Inc.). The excitation wavelength of DAPI was 405 nm. Hoechst was excited at 350 nm. LTR was excited at 561 nm and emitted at 570–590 nm. Lipi-Blue was excited at 405 nm and emitted at 450–500 nm. LTDR was excited at 640 nm and emitted at 668 nm. Images were processed and analyzed using the ImageJ software.

2.8. Cellular uptake assay

HepG2 cells were stained with 10 μM FITC-MOS-1 under different conditions: 1) the cells were stained with FITC-MOS-1 at 37 °C for 30 min; 2) the cells were stained with FITC-MOS-1 at 4 °C for 30 min; and 3) the cells were pre-incubated with NH_4Cl (50 mM) in FBS-free DMEM at 37 °C for 1 h and then incubated with FITC-MOS-1 at 37 °C for 30 min.

2.9. HepG2 high-fat model

HepG2 cells were seeded at a density of 1×10^5 on 35 mm glass-bottom culture dishes and incubated with 2 mL of DMEM with 10% (*V*/*V*) FBS for 24 h incubation (5% CO_2, 37 °C). Treatment of cells with 200 μM sodium oleate for 24 h induced steatosis and HepG2 high-fat model without causing a significant decrease in HepG2 cell viability.

2.10. Determination of TG in HepG2 cells

HepG2 cells (5×10^6 cells/mL) were incubated with different concentrations of MOS-1 for 6 h. Next, the TG content was determined using commercial assay kits according to the manufacturer's instructions (Biotopped, Beijing, China). Three secondary wells were used for each group.

2.11. Western blot

Cell samples were washed twice with PBS twice on ice, followed by lysis with radio immunoprecipitation assay (RIPA) buffer containing protease and phosphatase inhibitors. The collected lysates were kept on ice for 15–30 min followed by centrifugation for 15 min at 12,000 rpm at 4 °C. The supernatants were subjected to the bicinchoninic acid assay (BCA) protein assay kit (EpiZyme Inc., Shanghai, China) to determine total protein concentrations. For mice tissue samples, the mice were killed at the end of experiment, and tissues were snap-frozen in liquid nitrogen and minced via mortar and pestle, before storing at −80 °C. For Western blot protein sample preparation, frozen tissue powder was lysed with RIPA buffer containing protease and phosphatase inhibitors. The homogenates were centrifuged and the supernatants were collected. The total protein concentrations were determined. To ensure that the densitometric data for all of the target proteins will be within the linear quantitative range, 15 μg of proteins were subjected to sodium dodecyl sulfate-polyacrylamide gel electrophoresis (SDS-PAGE) and immunoblotting.

2.12. Animal handling

Normal mice and apolipoprotein E ($ApoE$)$^{-/-}$ mice were provided by Beijing Weitong Lihua Experimental Animal Technology Co., Ltd. (Beijing, China). The animal experiments were approved by the Institutional Animal Care and Use Committee of Shandong Academy of Pharmaceutical Science, Jinan, China (Approval No.: IACUC-2021-006). We used an established *in vivo* model of NAFLD mice where $ApoE^{-/-}$ male mice fed with a high-fat diet (HFD) (10% lard, 20% sucrose, 10% egg yolk powder, 0.5% sodium cholate, and 59.5% conventional feed) for two weeks were chosen as the *in vivo* model of NAFLD, and normal male mice on basal diet for two weeks

were used as the healthy mice control. After two weeks of feeding on a HFD, the HFD group was administered MOS-1 (0.2 g/kg) by gavage once a day for six weeks, based on the weight of the mice. The mice were weighed weekly. After the experiment, the mice were weighed and anesthetized with 1% (*V*/*V*) pentobarbital solution (30 mg/kg). Blood was drawn from the abdominal aorta and the mice in each group were dissected. The livers were taken out completely and the liver surfaces were washed with normal saline. A part of each liver was put into a pathological section box and fixed in 4% (*V*/*V*) paraformaldehyde solution, followed by section staining observation.

2.13. Plin2-mCherry transfection

Approximately 24 h before transfection, cells were seeded at a density of 2×10^5 cells per well in 3.5 cm glass bottom confocal dishes containing complete culture medium. Transfection was performed using the RFect Plasmid (BIOG, Changzhou Biogenerating Biotechnology Corp., Changzhou, China) according to the maunfacturer's protocol. The Plin2-mCherry plasmids (3.2 μg) and 200 μL of transfection buffer (Trans buffer) were mixed and incubated at room temperature for 5 min. At the same time, 20 μL of RFect was mixed with 200 μL of Trans buffer and incubated at room temperature for 5 min. The DNA-Trans and RFect-Trans buffers were then mixed together and incubated at room temperature for 15 min. The DNA-RFect-Trans buffer mixture was added dropwise to the cell culture medium and the cells were incubated in a cell culture incubator for 24 h.

2.14. Data analysis

Statistical analyses were performed using Origin 2021, GraphPad Prism 8, and ImageJ softwares. A normality test was used to check for normal distribution. In the case of normal distribution, the statistical comparison of results was test with a Student's t-test. In the case of non-normal distribution, the statistical comparison of results was test with a Mann-Whitney test, with levels of significance set at no significant difference (n.s.), $^{*}P < 0.05$, $^{**}P < 0.01$, $^{***}P < 0.001$, and $^{****}P < 0.0001$. Data are presented as mean ± standard deviation (SD).

3. Results and discussion

3.1. In vitro optical characterization and evaluation of biocompatibility of FITC-MOS-1

We prepared low-molecular-weight mussel oligosaccharides with degrees of 1–5, named MOS-1, from an enzymatically digested product of MP-A. We decided to characterize these low-molecular-weight saccharides to maximize their bioavailability and biological effects.

To visualize the subcellular distribution of MOS-1 and perform preliminary investigations of its bioactivity, we labeled MOS-1 with FITC (Fig. 1A and Scheme S1), as confirmed using HRMS (Figs. S1 and S2). Successful conjugation of MOS-1 and FITC was characterized via nuclear magnetic resonance spectroscopy (Figs. S3–S6). When the absorbance and fluorescence spectra of FITC, MOS-1, and FITC-MOS-1 were generated, the spectra of FITC-MOS-1 were found to be consistent with the presence of FITC, in that the spectra of both FITC-MOS-1 and free FITC had a strong absorption peak at 480 nm and a fluorescence emission peak at 530 nm (Figs. 1B, 1C, S7, and S8).

Cytotoxicity assays in HepG2 cells confirmed the biocompatibility of FITC-MOS-1 and suggested that it is relatively safe to administer *in vivo*. Specifically, CCK-8 assays showed no significant

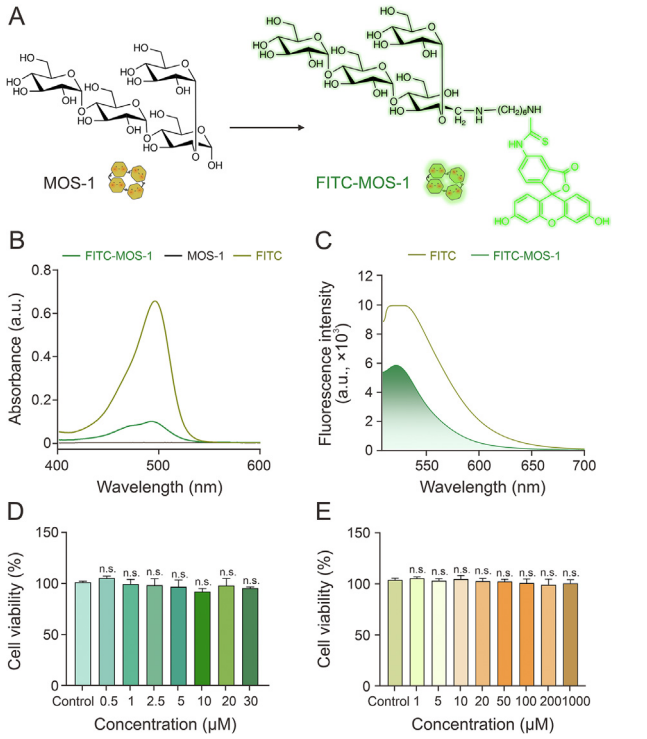

Fig. 1. Optical characterization and evaluation of the *in vitro* biocompatibility of fluorescein isothiocyanate (FITC)-mussel oligosaccharide (MOS-1). (A) Chemical structures of MOS-1 and FITC-MOS-1. (B) Ultraviolet-visible (UV-vis) absorption spectra of FITC, MOS-1, and FITC-MOS-1 (10 μM) in phosphate-buffered saline (PBS) containing 1% dimethyl sulfoxide (DMSO). (C) Fluorescence spectra of FITC and FITC-MOS-1 (10 μM) in PBS containing 1% DMSO (λ_{ex} = 488 nm). (D, E) The relative viability of HepG2 cells incubated with FITC-MOS-1 (D) or MOS-1 (E) or with vehicle (control). n.s.: no statistically significant.

decrease in viability in cells treated with up to 30 μM FITC-MOS-1 (Fig. 1D). Additionally, treatment with unlabeled MOS-1 showed no toxicity, even at higher concentrations (Fig. 1E), substantiating the suitability of FITC-MOS-1 for long-term imaging of dynamic processes in living cells.

3.2. Cell permeability of FITC-MOS-1

To test the ability of MOS-1 to cross the cell membrane, FITC-MOS-1 (10 μM) was incubated with HepG2 cells for 0.5, 1, 6, and 12 h prior to confocal imaging performed in the single-channel mode with excitation at 488 nm. As shown in Fig. 2A, after 0.5 h of incubation with FITC-MOS-1, an obvious green fluorescence signal was found to be evenly distributed in the cytoplasm in a pattern consistent with the presence of globular particles. The fluorescence intensity was enhanced with prolonged incubation time (Fig. 2B), suggesting that MOS-1 could enter cells in a time-dependent manner.

Quantitative analysis of fluorescence intensity confirmed the rapid uptake of FITC-MOS-1 by HepG2 cells within 0.5 h. To establish that FITC does not influence the permeability of MOS-1, we treated the cells with FITC dye alone. Fig. S9 shows that only a limited amount of the FITC dye was translocated across the cell membrane, resulting in sparse cytoplasmic distribution. These findings suggest that the entry of FITC-MOS-1 into the cytoplasm is primarily attributed to MOS-1 and is independent of the FITC dye alone. The flow cytometry results also revealed that FITC-MOS-1 was rapidly taken up by HepG2 cells in the time- and concentration-dependent manners (Figs. S10 and S11).

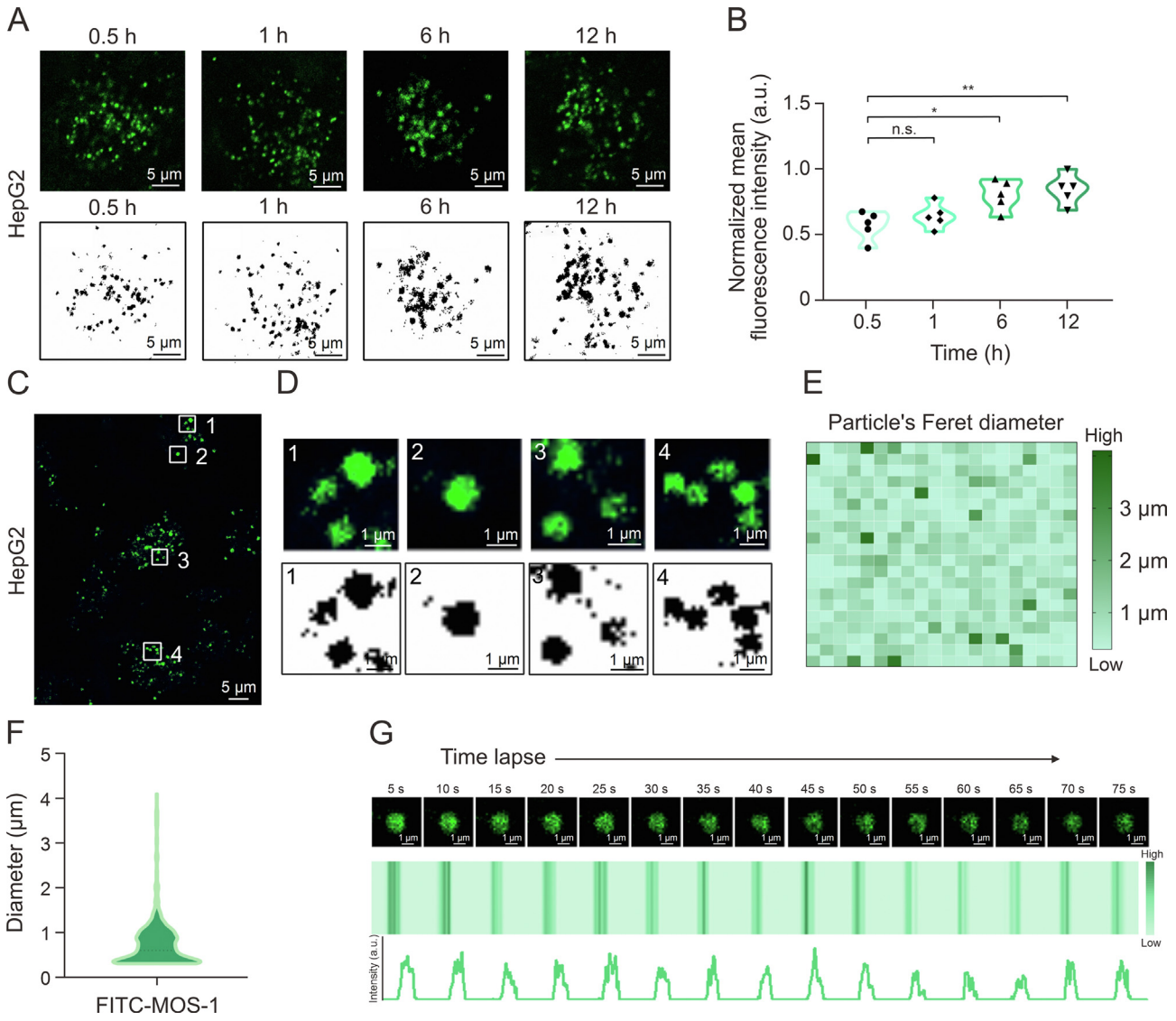

Fig. 2. Visualization of fluorescein isothiocyanate (FITC)-mussel oligosaccharide (MOS-1) distribution in living cells. (A) Confocal fluorescence images of HepG2 cells incubated with FITC-MOS-1 (10 μM) for 0.5, 1, 6, and 12 h. (B) The mean fluorescence intensity in cells from the samples shown in Fig. 2A ($n = 5$). (C) Confocal images of HepG2 cells stained with FITC-MOS-1 (10 μM) for 0.5 h. (D) (D) Enlarged view of areas of FITC-MOS-1 surrounded by the white rectangles numbered 1–4 in Fig. 2C: fluorescent puncta of FITC-MOS-1 (up) and extraction of fluorescent puncta (down). The numbers 1–4 in Figs. 2C and D indicate the typical distribution pattern of FITC-MOS-1 in HepG2. (E, F) Size distribution of the puncta labeled with FITC-MOS-1: heat map (E) and the particle distribution map (F) of the FITC-MOS-1 puncta ($n = 400$). (G) The time-dependent fluorescence intensity of FITC-MOS-1 upon continuous irradiation ($\lambda_{ex} = 488$ nm). $^{*}P < 0.05$ and $^{**}P < 0.01$; n.s.: no statistically significant.

In higher magnification confocal microscopic images of cells incubated with FITC-labeled MOS-1 (10 μM) for 0.5 h, distinct green fluorescence was observed in the form of well-dispersed circular spots (Figs. 2C, 2D, and S12). We conducted a co-localization study using DAPI as a nuclear stain, which demonstrated that FITC-MOS-1 particles were dispersed throughout the cytoplasm, as shown in Fig. S13. Additionally, we utilized super-resolution imaging to investigate the distribution of FITC-MOS-1 within the cells (Fig. S14). A size distribution analysis demonstrated that the diameters of these particles ranged from 0 to 2 μm (Figs. 2E and F), consistent with typical characteristics of lysosomes as previously reported [11]. As shown in Fig. S15, compared to 37 °C, low temperature at 4 °C and treatment with the endocytosis inhibitor (NH_4Cl) reduced the uptake of FITC-MOS-1, thus demonstrating that the entry of MOS-1 into the cell is energy-dependent.

To track the movement of MOS-1 in living cells, we exploited the high photostability of FITC and investigated the intracellular photostability during long-term excitation under confocal imaging conditions (Fig. 2G). The distinct intracellular fluorescence of FITC-MOS-1 remained relatively stable during excitation (>75 s), suggesting that this fluorescent labeling strategy is suitable for investigating the subcellular distribution of MOS-1.

3.3. Subcellular localization of FITC-MOS-1 in HepG2 cells

Based on the distribution of FITC-MOS-1 and the size of the fluorescent granules that appeared upon staining, we speculated that FITC-MOS-1 was localized in lysosomes [14]. To test this hypothesis, we co-stained cells with FITC-MOS-1 and a commercially available lysosomal probe, LTR [29], before performing confocal microscopy in the dual-channel mode with excitation at 488 nm (FITC-MOS-1) and 561 nm (LTR). As expected, the green fluorescent signal overlapped well with the red signals (Figs. 3A and B). The fluorescence intensity curves and 3D distribution map showed high

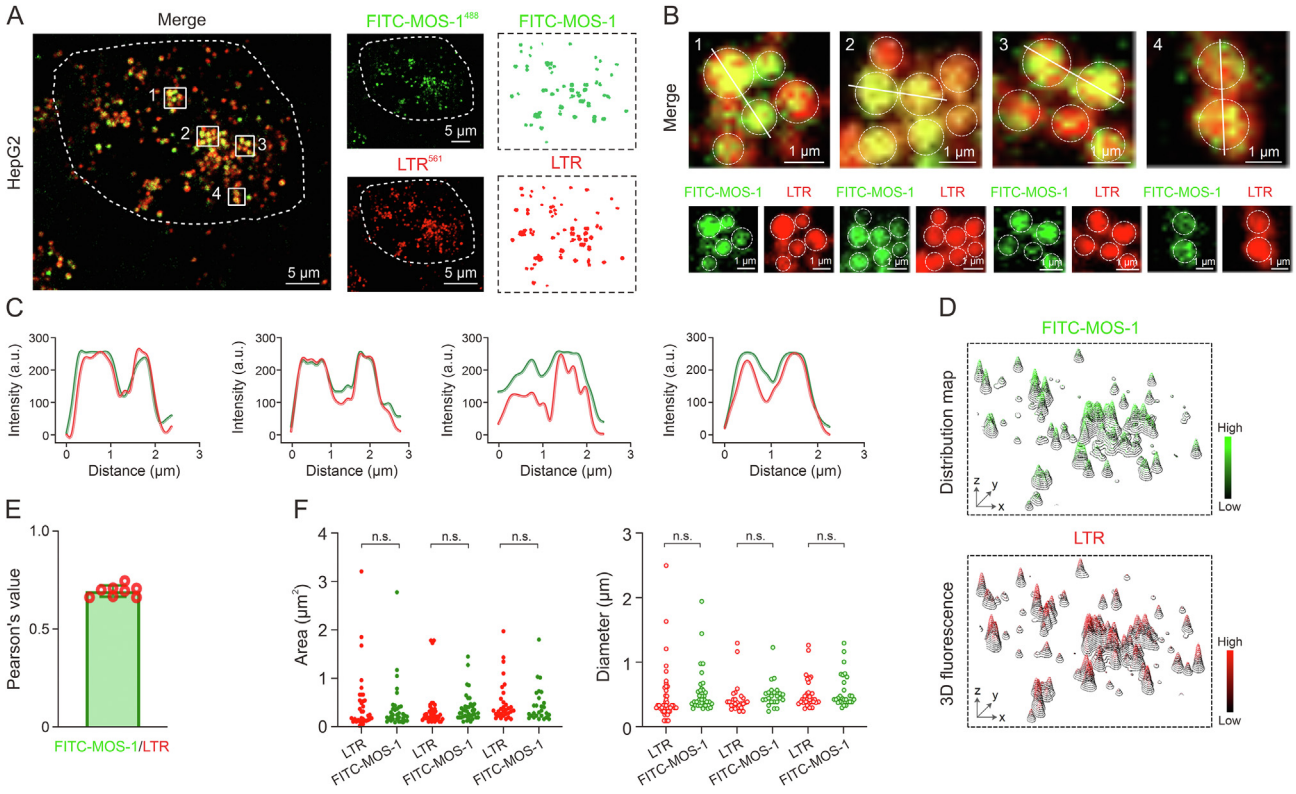

Fig. 3. Subcellular localization of fluorescein isothiocyanate (FITC)-mussel oligosaccharide (MOS-1) in HepG2 cells. (A) HepG2 cells were treated with FITC-MOS-1 (green) and LysoTracker Red (LTR; red). Areas of co-localization are visible in yellow, some of co-localization area were marked by white rectangles named 1–4. (B) Zoom-in images are an area surrounded by the white rectangles numbered 1–4 in Fig. 3A.. (C) Fluorescence intensity profiles of linear regions marked in Fig. 3B (green: FITC-MOS-1 and red: LTR). (D) Three-dimensional (3D) fluorescence distribution maps of FITC-MOS-1 and LTR in HepG2 cells. (E) Co-localization values for FITC-MOS-1 and LTR ($n = 8$). (F) Area and diameter analyses of FITC-MOS-1 and LTR in a population of cells ($n = 30$). n.s.: no statistically significant.

consistency between FITC-MOS-1 and LTR, with a Pearson's co-localization coefficient (PCC) of 0.7, implying that FITC-MOS-1 could penetrate the cell membrane and was uniformly distributed in the lysosomes (Figs. 3C–E). The results of super-resolution microscopy imaging led to the same conclusions (Fig. S16).

Next, we assessed the area and diameter of the punctate fluorescence representing the lysosome and FITC-MOS-1 and found no significant difference between the values of LTR and FITC-MOS-1 puncta (Fig. 3F). The subcellular distribution of FITC-MOS-1 was further investigated in other cell lines, including HeLa, U251, and MDA-MB-231, in which the FITC-MOS-1 signal exhibited a high co-localization with LTR (Fig. S17). These results support the conclusion that FITC-MOS-1 is localized in lysosomes.

To assess whether MOS-1 interacts with other organelles, we co-stained HepG2 cells with FITC-MOS-1 and other commercial probes, including a nuclear probe (Hoechst), a probe for lipid droplets (Lipi-Blue), and a mitochondrial probe (MTR). The results demonstrated that FITC-MOS-1 did not enter the other organelles (Figs. S18–S20). Accordingly, we hypothesized that MOS-1 alters the function of lysosomes and influences the related cell signaling pathways.

3.4. Alteration of lipophagy of high-fat HepG2 cells by FITC-MOS-1

We studied the bioactivity of MOS-1 in hepatocytes by investigating the effects of FITC-MOS-1 treatment on the dynamics of lysosomes and lipid droplets in a high-fat HepG2 cell model (Fig. S21). Confocal microscopy revealed clear changes in the distribution of lysosomes (red particles) and lipid droplets (blue particles) after FITC-MOS-1 incubation for 12 h (Fig. 4A), indicating that FITC-MOS-1 influences the interactions between lysosomes and lipid droplets. In control cells, we observed that lipid droplets were evenly distributed throughout the cytoplasm and lysosomes were situated near the cell center, with negligible co-localization of blue (nuclei) and red (lipid droplet membranes) signals. To determine the exact subcellular locations of lysosomes and lipid droplets, we utilized DAPI for nuclear staining and LTDR for lysosome staining. Additionally, we transfected Plin2-mCherry to specifically mark lipid droplets, as shown in Fig. S22. Our results consistently indicated minimal interactions between lysosomes and lipid droplets in high-fat HepG2 cells. In contrast, in cells treated with FITC-MOS-1, the lipid droplets were more concentrated in the region containing lysosomes, and co-localization of the red and blue regions was increased (Figs. 4B and C). Treatment with FITC alone did not significantly affect the proximity or interactions between the lysosomes and lipid droplets (Fig. S23).

We also used super-resolution imaging to investigate the interactions between lysosomes and lipid droplets [12,30,31] upon treatment with FITC-MOS-1 (Fig. S24). Here, we found that the average number of lysosomes per cell significantly increased in the FITC-MOS-1-treated group. After 12 h of treatment with FITC-MOS-1, the average distance between lipid droplets and lysosomes in the HepG2 cells decreased dramatically (Fig. 4D), and the co-localization of lipid droplets and lysosomes increased, with the value of PCC changing from 0.05 ± 0.04 in control cells to 0.34 ± 0.10 in treated cells ($P < 0.05$; Fig. 4E). The phenomenon was more vividly illustrated by the schematic diagram depicting lipid droplets and lysosomes (Fig. 4F).

The increased association between lysosomes and lipid droplets suggested that treatment with MOS-1 might influence lipophagy, a

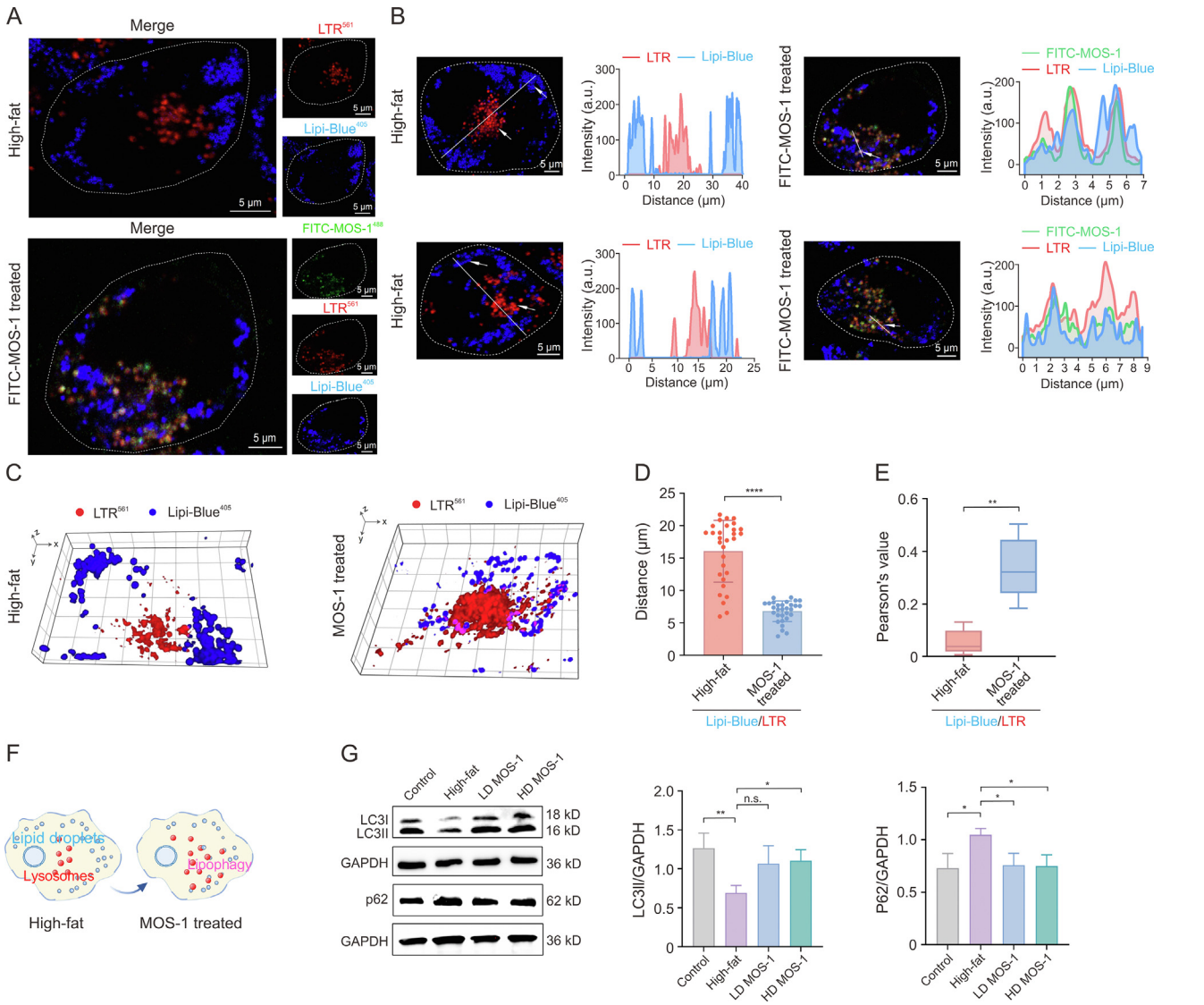

Fig. 4. The mechanism of regulation of lipophagy by fluorescein isothiocyanate (FITC)-mussel oligosaccharide (MOS-1) in high-fat HepG2 cells. (A) Confocal images showing the distribution of lipid droplets and lysosomes in high-fat HepG2 cells with or without FITC-MOS-1 treatment for 12 h: FITC-MOS-1 (green), Lyso-Tracker Red (LTR; red), and lipid droplets dyes (Lipi-Blue; blue). (B) Intensity profiles indicating that contact between lysosomes and lipid droplets in model group and FITC-MOS-1 treated group: FITC-MOS-1 (the green lines), LTR (the red lines), and Lipi-Blue (the blue lines). (C) Three-dimensional (3D) distribution map of lysosomes and lipid droplets in high-fat HepG2 cell with or without MOS-1 treatment for 12 h. (D) The distance between lysosomes and lipid droplets varies between untreated and MOS-1 treated groups in high-fat HepG2 cells. (E) Co-localization values for lysosomes and lipid droplets in model group and MOS-1 treated groups ($n = 5$). (F) Schematic representing changes to the distribution of lysosomes and lipid droplets under MOS-1 treatment. (G) Western blot analyses of LC3 and p62 expression between untreated and MOS-1 treated for 12 h. Panels in the middle and right show quantification of signal normalized to GAPDH expression ($n = 3$). $^{*}P < 0.05$, $^{**}P < 0.01$, and $^{****}P < 0.0001$; n.s.: no statistically significant. LD: low dose; HD: high dose; GAPDH: glyceraldehyde-3-phosphate dehydrogenase.

newfound pathway involved in the regulation of lipid metabolism [32–34]. During this process, lysosomes capture lipid droplets, leading to the degradation of TGs by lysosomal lipases. To further test this connection, we performed Western blotting to measure the cellular levels of p62, which is a marker of increased lipophagy, and of LC3II, which is a marker of decreased lipophagy. Here, we found that the normalized level of p62 was increased in high-fat model HepG2 cells relative to control HepG2 cells and that the normalized level of LC3II was decreased in the model cells (Fig. 4G). These results suggested that lipophagy is decreased in model cells relative to control cells. We next investigated whether the decreased level of lipophagy flux in the model cells was rescued upon treatment with low- or high-doses of MOS-1. In high-fat model cells treated with a high dose of MOS-1, we observed a significant decrease in the normalized level of p62 and an increase in the normalized level of LC3II relative to untreated high-fat model cells, indicating the restoration of lipophagy flux (Fig. 4G). This increased flux was consistent with the imaging results, which demonstrated an induction of the association between lysosomes and lipid droplets upon treatment with FITC-MOS-1 for 12 h.

3.5. MOS-1 reduced TG levels in high-fat HepG2 cells

Inspired by the discovery that lipophagy is promoted by MOS-1, we sought to investigate whether treatment with MOS-1 could influence TG levels in high-fat HepG2 cells. Therefore, we investigated the effect of incubation with MOS-1 ranging from 10 μM to 1 mM for 12 h on lipid metabolism in high-fat HepG2 cells. In

untreated cells, confocal imaging revealed the presence of numerous lipid droplets distributed around the cell and showed limited co-localization with lysosomes in the central region. In contrast, in cells treated with MOS-1 for 12 h, co-localization of lysosomes and lipid droplets was significantly increased in a dose-dependent manner, consistent with activation of the lipophagy process by MOS-1 (Fig. 5A).

We also analyzed the area, diameter, and the numbers of lipid droplets and lysosomes among different groups (Figs. 5B and C). The number of lysosomes gradually increased with increasing MOS-1 concentrations, whereas the number of lipid droplets decreased with increasing MOS-1 concentration. This pattern is consistent with a model in which lipophagy is promoted by MOS-1, leading to a decrease in the amount of lipid present in droplets and a corresponding increase in the mass of lysosomes.

In addition, we measured the effect of treatment with MOS-1 for 12 h on the lipid content of high-fat HepG2 cells and observed that the level of TGs present in these hepatocytes significantly decreased with MOS-1 treatment in a dose-dependent manner (Fig. 5D), in a pattern similar to that observed for lipid droplets. These findings provide compelling evidence that MOS-1 can reduce TG levels in hepatocytes by activating lipophagy.

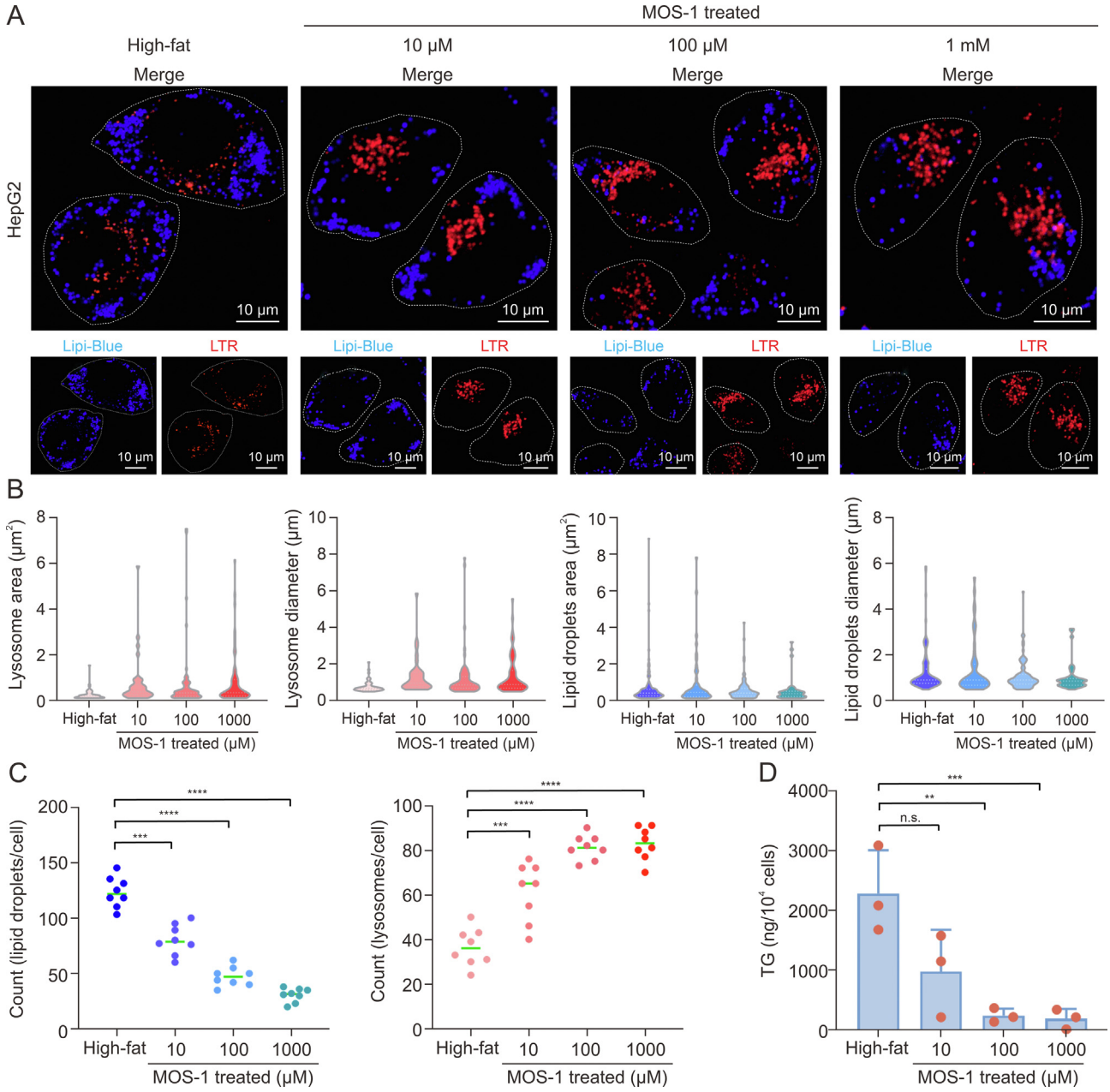

Fig. 5. Mussel oligosaccharide (MOS-1) reduced triglyceride levels in high-fat HepG2 cells. (A) Confocal imaging of high-fat model cells treated with the noted concentrations of unlabeled MOS-1 for 12 h: Lyso-Tracker Red (LTR, red) and lipid droplets dyes (Lipi-Blue; blue). (B) Area and particle diameter analyses of lipid droplets and lysosome in untreated and MOS-1-treated HepG2 cells ($n = 30$). (C) Counts of lipid droplets (left) and lysosomes (right) per cell in untreated cells and cells treated with different concentrations of MOS-1 ($n = 8$). (D) Triglyceride (TG) levels in untreated cells and cells treated with different concentrations of MOS-1 for 12 h ($n = 3$). $^{**}P < 0.01$, $^{***}P < 0.001$, and $^{****}P < 0.0001$; n.s.: no statistically significant.

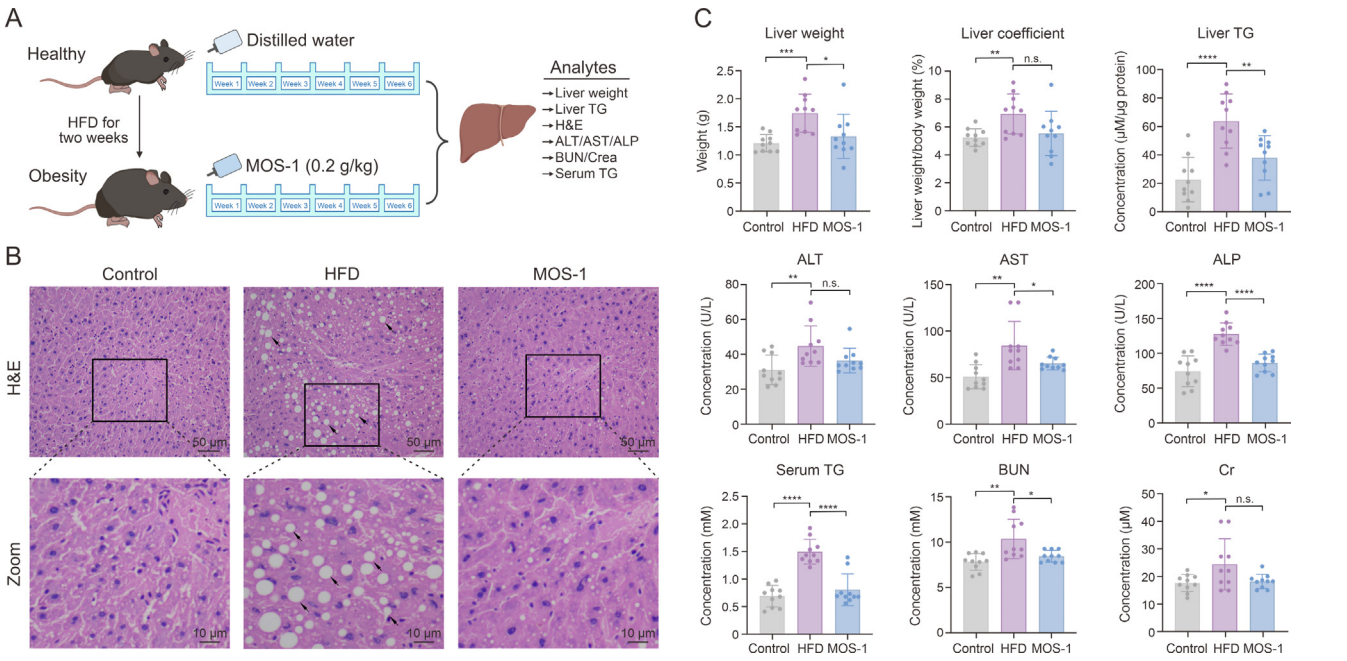

Fig. 6. Treatment with mussel oligosaccharide (MOS-1) reverses liver steatosis in mice fed a high-fat diet (HFD). (A) Time chart of animal experiment with gavage of MOS-1. (B) Representative hematoxylin and eosin (H&E) stains of mouse liver tissue sections. The black frame indicates the area shown in enlarged form in the bottom panelslack arrows indicate lipid droplets or microvesicular steatosis. (C) HFD-fed apolipoprotein E ($ApoE$)$^{-/-}$ mice were sacrificed after treatment with MOS-1 or vehicle control for two weeks, and values associated with liver status were determined according to standard methods. (n = 10 animals per group). $^{*}P < 0.05$, $^{**}P < 0.01$, $^{***}P < 0.001$, and $^{****}P < 0.0001$; n.s.: no statistically significant. TG: triglyceride; ALT: serum alanine transaminase; AST: serum aspartate aminotransferase; ALP: serum alkaline phosphatase; BUN: blood urea nitrogen; Crea: creatinine.

3.6. Alleviation effect of MOS-1 on NAFLD in HFD mice

The influence of MOS-1 on lipophagy and TG levels in high-fat HepG2 cells led us to further investigate the *in vivo* efficacy of MOS-1 using $ApoE^{-/-}$ mice maintained on a HFD (Fig. 6A). Liver tissue was evaluated using hematoxylin and eosin (H&E) staining. In liver sections isolated from HFD mice, we observed accumulation of lipid droplets and enlarged hepatocytes relative to those in tissues from the normal group. In contrast, treatment with MOS-1 significantly reversed this effect, reducing lipid droplet accumulation and alleviating microvesicular steatosis (Fig. 6B). To corroborate the changes in autophagy observed in HepG2 hepatocytes *in vitro*, we examined the autophagic activity in mice fed a HFD and in those receiving treatment. We observed a significant decrease in LC3II levels in HFD mice, suggesting an impairment of autophagic flux. However, MOS-1 treatment markedly ameliorated this impairment (Fig. S25). After one week of adaptation on a normal diet, $ApoE^{-/-}$ mice were fed a high-fat diet for two weeks. MOS-1 treatment significantly reduced liver weight (Fig. 6C) in HFD-fed mice, while the ratio of liver weight to body weight (liver coefficient) showed no significant difference (Fig. 6C). To further investigate the correlation between liver weight and liver TG levels, we quantified liver TG levels in the total liver lysates. In HFD-fed mice, the levels of TGs in the liver were significantly increased compared to those in mice fed a normal diet, indicating that a HFD induces the accumulation of TGs within the liver, correlating with increased liver weight. However, treatment of mice fed a HFD with MOS-1 led to a significant reduction in liver TG levels, demonstrating that MOS-1 treatment could relieve effect of a HFD. Furthermore, we analyzed liver function indices, including plasma aspartate aminotransferase (AST), alanine aminotransferase (ALT), and alkaline phosphatase (ALP), as well as routine indices of kidney function, blood urea nitrogen (BUN), and creatinine (Crea). In the HFD group, these indices were significantly elevated compared to those in the normal diet group. However, after six weeks of MOS-1 treatment, most of these indices in the treatment group were significantly decreased compared to those in the model group (Fig. 6C).

Additionally, serum TG levels were significantly higher in the model group than in the normal group (Fig. 6C), consistent with previous reports [35] and confirming the successful induction of the model. Remarkably, treatment of the model mice with MOS-1 (0.2 g/kg) by gavage once daily for six weeks led to a significant decrease in serum TG levels compared to treatment with the vehicle control. The resulting TG levels were not significantly different from those of control fed on a normal diet (Fig. 6C).

Collectively, our findings demonstrate that MOS-1 decreases the accumulation of TGs in the liver, ameliorates hepatic steatosis, and improves hepatic function, making it a promising candidate for the treatment of NAFLD.

4. Conclusion

In this study, we employed a strategy for the *in situ* visual monitoring of MOS-1, allowing us to track its subcellular localization and distribution in real time. Our findings demonstrate that MOS-1 localizes to lysosomes and actively recruits lipid droplets, leading to fusion events and consumption of cellular lipid components. These results suggest that MOS-1 is a promising candidate for the treatment of lipid-related diseases. The effect of MOS-1 on lipid metabolism was further corroborated by experiments conducted at both the cellular and animal levels, which revealed that MOS-1 significantly promoted lipid droplet degradation, reduced lipid droplet abundance, lowered serum TG levels, and mitigated liver damage and steatosis, thus demonstrating its potential application in the treatment of lipid-related diseases.

This research underscores the importance of *in situ* visual monitoring of drug localization and distribution within subcellular compartments during drug development. By directly observing and monitoring drug dynamics in cells, we can gain a more precise understanding of the mechanisms of action and efficiently identify appropriate research targets and indications. This method holds significant value for the screening and development of selective small-molecule drugs and is poised to expedite the discovery of candidate molecules with therapeutic efficacy.

Overall, this study provides compelling evidence regarding the functional and mechanistic aspects of mussel oligosaccharides and highlights their potential therapeutic applications in the treatment of NAFLD. However, further investigations are warranted to thoroughly evaluate the pharmacological and toxicological properties of mussel oligosaccharides. We believe that this study lays a solid foundation for the continued development and utilization of mussel oligosaccharides, offering valuable insights into similar strategies for the investigation of other NPs. Ultimately, these efforts hold promise for catalyzing groundbreaking advancements in the fields of disease treatment and drug development.

CRediT author statement

Zhenjie Yu: Investigation, Formal analysis, Writing - Original draft preparation; **Huarong Shao**: Validation, Writing - Original draft preparation; **Xintian Shao**: Methodology, Visualization; **Linyan Yu:** Supervision, Validation; **Yanan Gao**: Software, Formal analysis; **Youxiao Ren**: Data curation, Investigation; **Fei Liu**: Validation, Methodology; **Caicai Meng**: Supervision, Writing - Reviewing and Editing; **Peixue Ling** and **Qixin Chen**: Writing - Reviewing and Editing.

Declaration of competing interest

The authors declare that there are no conflicts of interest.

Acknowledgments

This work was financially supported by Shandong Province Key R&D Program, China (Major Technological Innovation Project) (Grant No.: 2021CXGC010501), Young Elite Scientists Sponsorship Program by China Association of Chinese Medicine, China (Grant No.: CACM-2023-QNRC1-02), the National Natural Science Foundation of China (Grant Nos.: 22107059, 22007060, and 82302743), the Natural Science Foundation of Shandong Province, China (Grant Nos.: ZR2022QH304, ZR2021QH057, and ZR2020QB166), the Program for Youth Innovation Technology in Colleges and Universities of Shandong Province of China (Grant No.: 2021KJ035), Taishan Scholars Program, China (Grant Nos.: TSQN202211221 and TSPD20181218), Shandong Science Fund for Excellent Young Scholars, China (Grant No.: ZR2022YQ66), Shandong Province Traditional Chinese Medicine Science and Technology Project, China (Grant No.: Q-2023059), Shenzhen Basic Research Project, China (Grant No.: JCYJ20190809160209449), the General Project of Shandong Natural Science Foundation, China (Grant No.: ZR2021MH341), and Jinan Innovation Team Project of Colleges and Universities, China (Grant No.: 2021GXRC072).

Appendix A. Supplementary data

Supplementary data to this article can be found online at https://doi.org/10.1016/j.jpha.2023.12.022.

References

[1] D.J. Newman, G.M. Cragg, Natural products as sources of new drugs from 1981 to 2014, J. Nat. Prod. 79 (2016) 629–661.
[2] S.E. Motika, P.J. Hergenrother, Re-engineering natural products to engage new biological targets, Nat. Prod. Rep. 37 (2020) 1395–1403.
[3] M. Fu, X. Han, B. Chen, et al., Cancer treatment: From traditional Chinese herbal medicine to the liposome delivery system, Acta Mater. Med. 1 (2022) 486–506.
[4] Y. Bai, C. Yang, N. Deng, et al., Design and synthesis of novel 7-ethyl-10-fluoro-20-O-(cinnamic acid ester)-camptothecin derivatives as potential high selectivity and low toxicity topoisomerase I inhibitors for hepatocellular carcinoma, Biochem. Pharmacol. 200 (2022), 115049.
[5] B. Waltenberger, A. Mocan, K. Šmejkal, et al., Natural products to counteract the epidemic of cardiovascular and metabolic disorders, Molecules 21 (2016), 807.
[6] R. Toy, L. Bauer, C. Hoimes, et al., Targeted nanotechnology for cancer imaging, Adv. Drug Deliv. Rev. 76 (2014) 79–97.
[7] A.R. Carroll, B.R. Copp, R.A. Davis, et al., Marine natural products, Nat. Prod. Rep. 39 (2022) 1122–1171.
[8] J. Sun, C.-Y. Yan, J. Niu, et al., Latent herpes simplex virus type 1 reactivation increases the susceptibility of neurodegenerative diseases: intervention with traditional Chinese medicine, Acta Mater. Med. 1 (2022) 534–551.
[9] G. Hu, Y. Su, B.H. Kang, et al., High-throughput phenotypic screen and transcriptional analysis identify new compounds and targets for macrophage reprogramming, Nat. Commun. 12 (2021), 773.
[10] D. Si, Q. Li, Y. Bao, et al., Fluorogenic and cell-permeable rhodamine dyes for high-contrast live-cell protein labeling in bioimaging and biosensing, Angew. Chem. Int. Ed. 62 (2023), e202307641.
[11] Q. Chen, H. Fang, X. Shao, et al., A dual-labeling probe to track functional mitochondria-lysosome interactions in live cells, Nat. Commun. 11 (2020), 6290.
[12] X. Shao, C. Meng, W. Song, et al., Subcellular visualization: organelle-specific targeted drug delivery and discovery, Adv. Drug Deliv. Rev. 199 (2023), 114977.
[13] L. Wang, M.S. Frei, A. Salim, et al., Small-molecule fluorescent probes for live-cell super-resolution microscopy, J. Am. Chem. Soc. 141 (2019) 2770–2781.
[14] L. Liu, H. Fang, Q. Chen, et al., Multiple-color platinum complex with super-large Stokes shift for super-resolution imaging of autolysosome escape, Angew. Chem. Int. Ed. Engl. 59 (2020) 19229–19236.
[15] H. Chen, H. Wang, Y. Wei, et al., Super-resolution imaging reveals the subcellular distribution of dextran at the nanoscale in living cells, Chin, Chem. Lett. 33 (2022) 1865–1869.
[16] Y. Wei, L. Kong, H. Chen, et al., Super-resolution image-based tracking of drug distribution in mitochondria of a label-free naturally derived drug molecules, Chem. Eng. J. 429 (2022), 132134.
[17] M. Swierczewska, H.S. Han, K. Kim, et al., Polysaccharide-based nanoparticles for theranostic nanomedicine, Adv. Drug Deliv. Rev. 99 (2016) 70–84.
[18] F. Liu, X. Liu, F. Chen, et al., Mussel-inspired chemistry: a promising strategy for natural polysaccharides in biomedical applications, Prog. Polym. Sci. 123 (2021), 101472.
[19] Z. Li, X. Feng, S. Luo, et al., High drug loading hydrophobic cross-linked dextran microspheres as novel drug delivery systems for the treatment of osteoarthritis, Asian J. Pharm. Sci. 18 (2023), 100830.
[20] Z.U. Arif, M.Y. Khalid, R. Noroozi, et al., Additive manufacturing of sustainable biomaterials for biomedical applications, Asian J. Pharm. Sci. 18 (2023), 100812.
[21] U. Grienke, J. Silke, D. Tasdemir, Bioactive compounds from marine mussels and their effects on human health, Food Chem. 142 (2014) 48–60.
[22] W. Lu, B. Guo, X. Wang, et al., The receptor for activated C kinase 1 (RACK1) mediating immune response in thick shell mussel Mytilus coruscus, Dev. Comp. Immunol. 85 (2018) 61–70.
[23] H.B. Vaidya, S. Gangadaran, S.K. Cheema, An obesogenic diet enriched with blue mussels protects against weight gain and lowers cholesterol levels in C57BL/6 mice, Nutr. Res. 46 (2017) 31–37.
[24] J. Wu, H. Shao, J. Zhang, et al., Mussel polysaccharide α-D-glucan (MP-A) protects against non-alcoholic fatty liver disease via maintaining the homeostasis of gut microbiota and regulating related gut-liver axis signaling pathways, Int. J. Biol. Macromol. 130 (2019) 68–78.
[25] X. Xiang, R. Wang, L. Yao, et al., Anti-inflammatory effects of *Mytilus coruscus* polysaccharide on $RAW_{264.7}$ cells and DSS-induced colitis in mice, Mar. Drugs 19 (2021), 468.
[26] X. Xiang, R. Wang, L. Chen, et al., Immunomodulatory activity of a water-soluble polysaccharide extracted from mussel on cyclophosphamide-induced immunosuppressive mice models, NPJ Sci. Food 6 (2022), 26.
[27] Y. Liu, C. Zhang, Y. Wei, et al., De Novo-Designed landmine warfare strategy luminophore for super-resolution imaging reveal $ONOO^-$ evolution in living cells, Chem. Eng. J. 422 (2021), 130151.
[28] G. Fang, H. Chen, X. Shao, et al., Single image capture of bioactive ion crosstalk within inter-organelle membrane contacts at nanometer resolution, Small Methods 6 (2022), e2200321.
[29] L. Wang, R. Chen, G. Han, et al., Super-resolution analyzing spatial organization of lysosomes with an organic fluorescent probe, Explorations (Beijing) 2 (2022), 20210215.

[30] Z. Ye, C. Hu, J. Wang, et al., Burst of hopping trafficking correlated reversible dynamic interactions between lipid droplets and mitochondria under starvation, Explorations (Beijing) 3 (2023), 20230002.
[31] C. Zhang, H. Shao, J. Zhang, et al., Long-term live-cell lipid droplet-targeted biosensor development for nanoscopic tracking of lipid droplet-mitochondria contact sites, Theranostics 11 (2021) 7767–7778.
[32] R. Singh, S. Kaushik, Y. Wang, et al., Autophagy regulates lipid metabolism, Nature 458 (2009) 1131–1135.
[33] N. Martinez-Lopez, R. Singh, Autophagy and lipid droplets in the Liver, Annu. Rev. Nutr. 35 (2015) 215–237.
[34] A. Grefhorst, I.P. van de Peppel, L.E. Larsen, et al., The role of lipophagy in the development and treatment of non-alcoholic fatty liver disease, Front. Endocrinol. 11 (2020), 601627.
[35] W. Tao, W. Sun, L. Liu, et al., Chitosan oligosaccharide attenuates nonalcoholic fatty liver disease induced by high fat diet through reducing lipid accumulation, inflammation and oxidative stress in C57BL/6 mice, Mar. Drugs 17 (2019), 645.